Progress in Additive Manufacturing (2026) 11:4061–4075
https://doi.org/10.1007/s40964-026-01567-1

RESEARCH

Feedstock characterization and process calibration for fused pellet fabrication of PLA/limestone composites

Joaquim Manoel Justino Netto[1] · Dora Sousa[1] · Pedro Amaral[1] · Marco Leite[1]

Received: 22 July 2025 / Accepted: 27 January 2026 / Published online: 17 February 2026

Abstract

Natural stone industry generates large volumes of mineral waste, whose valorization in polymer composites through 3D printing remains limited. This study explores the feedstock properties, calibration, and mechanical performance of poly(lactic acid) (PLA) composites with limestone using screw-assisted material extrusion. Neat PLA and composite pellets were characterized by differential scanning calorimetry, rheometry, and Fourier-transform infrared spectroscopy. Thermal analysis indicated that limestone promoted heterogeneous nucleation at moderate filler loading, whereas excessive incorporation disrupted crystallization due to reduced chain mobility. Rheological analysis revealed shear-thinning behavior for all formulations, with viscosity increase with limestone addition at higher angular frequencies and suppressed terminal elastic response at high filler content. Fourier-transform infrared spectroscopy suggested minor structural changes without significant signs of compounding-related degradation. A three-stage calibration process on a retrofitted 3D printer established fused pellet fabrication (FPF) process conditions. Mechanical tests showed higher limestone content increased stiffness, reaching an elastic modulus up to 4.3 GPa for the composite containing 50 wt.% of limestone, while reducing ductility and strength, consistent with values reported for filament-based fused filament fabrication. Overall, this work demonstrates the feasibility of processing PLA/limestone composites via desktop-scale FPF and highlights the importance of formulation-specific calibration. The findings support the potential upcycling of mineral waste from the stone industry into value-added, eco-friendly materials for additive manufacturing.

Keywords Highly filled polymers · Pellet extrusion · Process calibration · Circular economy

1 Introduction

Natural stone is renowned for its durability and versatility, having been used for centuries in construction, architecture, and for decorative arts. Today, the global stone industry continues to thrive, with Portugal ranking as the seventh-largest producer and exporter of natural stone, reaching €488 million in exports in 2023 [1]. However, alongside its economic relevance, the sector faces a pressing environmental challenge: managing stone sludge waste, a byproduct generated during cutting, polishing, and finishing operations, composed primarily of fine stone powder suspended in water [2].

One promising approach to valorize this mineral waste is its incorporation into thermoplastic composites. Mineral fillers are known to enhance the mechanical and thermal performance of polymers while also lowering production costs [3]. The comprehensive review by Fajdek-Bieda and Wróblewska [4] highlights how the addition of natural minerals in polymer matrices significantly influences processing conditions and final properties. In general, mineral-reinforced thermoplastics exhibit increased stiffness, hardness, dimensional and thermal stability, along with improved fire and weather resistance, albeit often at the expense of reduced ductility and impact strength [5–9]. Traditionally, polymers filled with small amounts of minerals are used in profile

✉ Joaquim Manoel Justino Netto
joaquim.netto@tecnico.ulisboa.pt

Dora Sousa
dsousa@tecnico.ulisboa.pt

Pedro Amaral
pedro.amaral@tecnico.ulisboa.pt

Marco Leite
marcoleite@tecnico.ulisboa.pt

[1] IDMEC, Instituto Superior Técnico, Universidade de Lisboa, Lisboa, Portugal

extrusion, film blowing, and injection molding to manufacture low value-added products for the construction, automotive, and packaging sectors [4].

In recent years, material extrusion additive manufacturing (MEX-AM) has emerged as a promising technique for the valorization of industrial waste, due to its simplicity and relatively low costs [10, 11]. Despite this potential, few studies have explored the use of stone waste composites as feedstock for extrusion-based 3D printing. Corcione et al. [12] assessed the environmental performance of limestone (LS), neat PLA, and PLA/LS composites containing 50 wt. % and 60 wt.% of LS waste powder through life cycle analysis (LCA) and examined their feasibility for fused filament fabrication (FFF). Although 3D printing was successful, the composites showed higher environmental impacts due to the energy demands related to PLA production, melt blending, and filament fabrication. However, the authors argue that substituting natural stone with PLA/LS composites could reduce quarrying and, by incorporating large amounts of stone waste, the need for virgin plastic production could be reduced. In a more recent study, Sousa et al. [13] processed neat PLA and composites containing 25 wt.% and 50 wt.% limestone into tensile specimens by injection molding and FFF, the latter approach also requiring the preparation of 1.75 mm diameter filaments. The injection-molded composites exhibited increased stiffness, reaching 3.4 GPa and 5.0 GPa for the 25 wt.% and 50 wt.% fillers, respectively, compared to 3.1 GPa for neat PLA, accompanied by a reduction in stress at break to 38.2 MPa and 34.0 MPa (vs. 42.5 MPa for neat PLA). The FFF specimens showed the same general trend, albeit with lower absolute values due to printing defects. The addition of limestone enhanced stiffness but reduced filament flexibility and printability, particularly at higher filler loadings.

Filament-related limitations can be overcome by directly using pellets or granular materials in screw-assisted 3D printers, which have been progressively developed and commercialized over the past decade. This approach, known as fused pellet fabrication (FPF), enables higher productivity through increased deposition rates and reduced feedstock costs, while also expanding the range of printable materials and allowing large-scale printing [14]. Several retrofit kits are now available that convert conventional FFF printers into FPF systems by replacing filament-based printheads with miniature screw extruders. The study by Fayazfar et al. [15] exemplifies the potential of such retrofitted systems to support distributed recycling of plastic bottles. Despite careful attention to feedstock formulation and characterization, the paper provides limited details on the 3D printing process, particularly concerning extruder calibration. This aspect is critical because, unlike filament-fed printers that control flow mainly through melt pressure and nozzle geometry, FPF systems must regulate material delivery arising from complex interactions among screw geometry, rotation speed, and pressure-induced backflow [16, 17]. As extrusion flow cannot be directly predicted as a function of screw speed for all screw designs, typical FFF slicing parameters must be carefully adjusted to ensure consistent deposition [18, 19].

One of the most critical parameters to adjust is the extrusion multiplier (EM), which originally modifies the length of filament fed to the print head defined by the value of the “E” command in the G-code [20]. A previous study on FPF with a custom-built single-screw printhead proposed an analytical modeling approach to calibrate EM based on the mass flow rate required to extrude and deposit a line of molten polymer with predefined geometry [21]. The model essentially sought to determine how much faster the screw-driving motor should rotate compared to a standard motor feeding a 1.75 mm filament. However, the predicted EM values diverged from experimental measurements, likely due to factors such as density variations between solid and molten polymer, temperature effects on the plastication process, and 3D printing parameters such as the nozzle–print bed standoff distance. In a subsequent study using the same setup, EM was instead empirically calibrated through cube-printing tests using two nozzle sizes [19].

Given the considerable volume of waste generated by the stone industry as well as the technical hurdles and energy expenditure associated with filament fabrication [22], the development of mineral-filled composites for use in screw-assisted 3D printers represents a promising yet underexplored research avenue. This study investigates the processing behavior and performance of pelletized PLA/limestone composites for FPF applications. Thermal, rheological, and chemical properties were evaluated for neat PLA and composites containing 25 wt.% and 50 wt.% limestone. These materials were subsequently used to calibrate FPF process parameters for the production of tensile specimens. Extrusion multiplier, layer height, and layer width were adjusted to ensure that the number and spacing of successive rasters reproduced the intended mesostructure. In addition to nozzle temperature, print speed, and nozzle diameter [19], the appropriate settings for these parameters depend strongly on the material’s flowability during processing. Therefore, considering the different material properties, FPF calibration was performed individually for each formulation.

By advancing the understanding of mineral-filled biopolymers processed via desktop FPF systems, this study contributes to the development of large-scale, pellet-based extrusion processes, promoting cost and energy reduction while offering a viable valorization pathway for mineral residues generated by the stone industry.

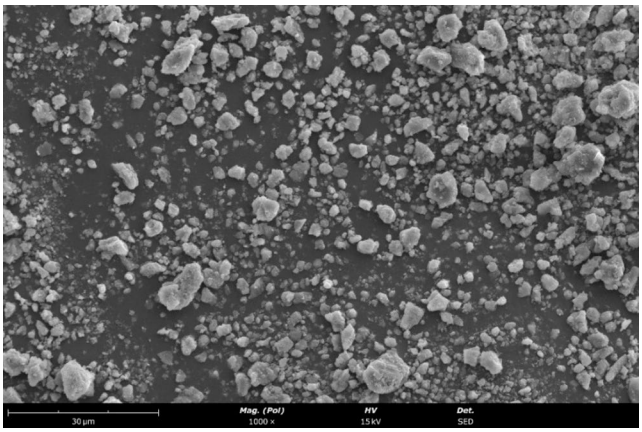

Fig. 1 Representative SEM image of the limestone powder after drying and sieving

2 Materials and methods

The PLA grade used as matrix, INZEA F2 HTS 451, is suitable for injection and extrusion applications and was purchased from Nurel Biopolymers (Zaragoza, Spain). It consists of a biodegradable and compostable material based on PLA and potato starch acetate (PSAC) [23]. The limestone powder was supplied as sludge by Filstone Comércio de Rochas, S.A. (Fátima, Portugal). The sludge, a byproduct of quarry extraction by diamond wire sawing, was dried and sieved through a 355 µm mesh to remove coarse agglomerates. A representative scanning electron microscopy (SEM) micrograph of the limestone powder, after drying and sieving, is shown in Fig. 1.

Particle size distribution (PSD) was determined by analysis of SEM images, as reported in a previous publication [13], using ImageJ v1.54 g software. At least 300 manual measurements of the particles' major axis were taken across multiple regions of the sample to ensure representative sampling. The analysis indicated that approximately 80% of the particles had sizes below 10 µm [13].

2.1 Feedstock production

The composites were produced using a Werner & Pfleiderer ZSK 25×38D co-rotating twin-screw extruder. Formulations containing up to 25 wt.% and 50 wt.% limestone powders were prepared, hereafter referred to as PLA/25LS and PLA/50LS, respectively. The barrel's heating zones were set according to the temperatures listed in Table 1, from the feeding hopper to the die. For all formulations, the twin-screw speed was maintained between 60 and 70 rpm. Following extrusion, the composites were cooled in a water tank and pelletized. The resulting pellets were stored in sealed plastic bags and conditioned at room temperature.

2.2 Feedstock characterization

A differential scanning calorimeter (Netzsch DSC 200 F3 Maia) was employed to investigate the thermal properties of virgin PLA and its composites. The samples were subject to two heating cycles conducted at a rate of 10 °C/min, over a temperature range of −20 to 250 °C, under nitrogen atmosphere with a flow rate of 50 mL/min. The thermal transitions were evaluated from the second heating cycles using the Netzsch Proteus DSC 200 F3 software (version 5.2.0, 2010). The degree of crystallinity (X_c) was calculated using Eq. 1 [24], based on the measured enthalpies of cold crystallization (ΔH_{cc}) and melting (ΔH_m) obtained from the DSC thermograms, assuming an enthalpy of melting for 100% crystalline PLA (ΔH_m^0) of 93.0 J/g [24].

$$X_c = \frac{(\Delta H_m - \Delta H_{cc})}{\Delta H_m^0} \times 100 \quad (1)$$

Small-amplitude oscillatory shear (SAOS) rheological tests were conducted using an Anton Paar MCR 92 rheometer equipped with 25 mm diameter parallel plates spaced by a 1 mm gap. To determine the linear viscoelastic region (LVR), strain sweep tests were first conducted at a constant angular frequency of 10 rad/s. Subsequently, frequency sweep tests were carried out within the LVR strain limit, covering a range from 0.1 to 500 rad/s at 200 °C, to evaluate the complex viscosity (η*), storage modulus (G'), and loss modulus (G'').

To perform Fourier Transform Infrared (FTIR) spectroscopy, sample pellets from the PLA/25LS and PLA/50LS composites were dissolved in HPLC-grade chloroform (Carlo Erba). After the limestone particles precipitated, the supernatant was carefully collected using a pipette and transferred to a Petri dish for solvent evaporation. The dried residue was then ground and analyzed using a Nicolet 5700 spectrometer (Thermo Electron Corporation), with 125 scans acquired per sample in transmittance mode. Samples of the virgin PLA and of the isolated limestone powder were also subject to FTIR spectroscopy in the same scanning conditions.

Table 1 Temperature profile used in the co-rotating twin-screw extruder to fabricate the composite pellets

Heating zone								
1	2	3	4	5	6	7	8	9
180ºC	177 ºC	175 ºC	170 ºC	168 ºC	173 ºC	165 ºC	168 ºC	168 ºC

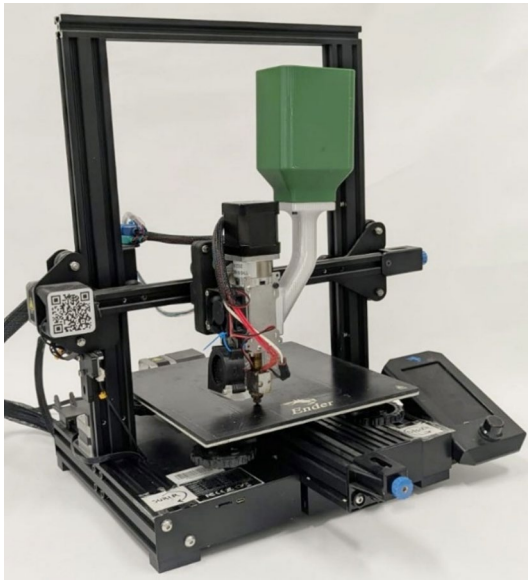

Fig. 2 Experimental 3D printing setup with the Mahor v4 pellet extruder

2.3 Determination of FPF parameters

The pellets were processed using a Mahor Pellet Extruder v4 printhead (Mahor.XYZ, Spain), mounted on a Creality Ender 3 v2 (Shenzhen Creality 3D Technology Co., China) platform, shown in Fig. 2.

The printhead consists of a miniature, vertical single-screw extruder with an 8 mm screw diameter and 50 mm screw length, that is driven by a NEMA 17 stepper motor connected to a 5:1 speed reducer. Pellet feeding was performed laterally using the aperture in the upper portion of the barrel, where a hopper was attached. The heating element was positioned around the barrel and near the 0.8 mm diameter hardened steel nozzle, as recommended by the supplier for low throughput [25]. Since the 3D printer did not present any Z probe, the reference for the origin of the Z-axis was established by placing a sheet of paper (approximately 0.08 mm) between the nozzle and the build plate. Bed levelling was performed manually by adjusting the corner levelling screws.

The feasible parameters for FPF were determined following a three-stage approach. In the first stage, screening extrusion tests were conducted to determine the valid range of feed rates, nozzle temperatures, and the resulting flow rates for each material. Nozzle temperature was set to 200 ºC, 220 ºC, and 240 ºC, while the feed rates were set to 10, 20, and 30 mm/s. For each material–temperature–feed rate combination, five one-minute extrusion samples were collected and weighed using an analytical balance (Kern PCB 1000-2). Volumetric throughput was calculated by dividing the measured mass by the material density, assuming the density of PLA as 1.23 g/cm^3 [26] and the density of limestone as 2.7 g/cm^3 [27], while the densities of the composites were estimated using the rule of mixtures. Analysis of variance (ANOVA) was performed using Minitab software to assess the statistical significance of the processing parameters.

Table 2 Factors studied to determine the effective layer height and width of vase-mode cubes printed using PLA, PLA/25LS, and PLA/50LS

Nomenclature	Print speed (mm/s)	Extrusion multiplier
PS10_EM3	10	3
PS10_EM4		4
PS30_EM3	30	3
PS30_EM4		4

In the second stage, the EM required to compensate for non-volumetric extrusion was determined by fabricating 20 mm cubes in vase mode, without bottom or top layers. EM values of 1, 2, 3, and 4 were tested at printing speeds of 10 mm/s and 30 mm/s, while keeping a constant nozzle temperature of 220 °C. EM values above 4 were not tested, as prior experience resulted in motor stalling. The nominal layer height and extrusion width were set to 0.6 mm and 1 mm, respectively, in the PrusaSlicer software. The printed cubes were examined using a digital microscope (model CAMCOLMS1). Suitable EM values were identified as those producing continuous, well-defined extruded lines. At this stage, only neat PLA was used, and the resulting EM values were assumed to be applicable to the composite formulations as well.

In the third stage, additional cubes were printed in vase mode to determine the effective layer height (h) and width (w) produced under different conditions for all three materials (*i.e.* PLA, PLA/25LS, and PLA/50LS). Two factors, namely print speed (PS), and EM, were varied at two levels each to assess their influence on the geometry of the extruded lines, keeping the nozzle temperature at 220 ºC. The nomenclature and corresponding values used for each parameter are listed in Table 2.

3D printing was performed with the nozzle and bed temperatures fixed at 220 ºC and 60 ºC, respectively, using the same nominal layer height and width (0.6 mm and 1 mm, respectively) in the slicing software. After printing, the cubes were fractured in liquid nitrogen, and cross-sectional images of the walls were captured using the digital microscope. At least ten measurements of layer height and width were taken from the fractured strands using ImageJ v. 1.54 g software. ANOVA tests were conducted on the measured strand dimensions using Minitab software.

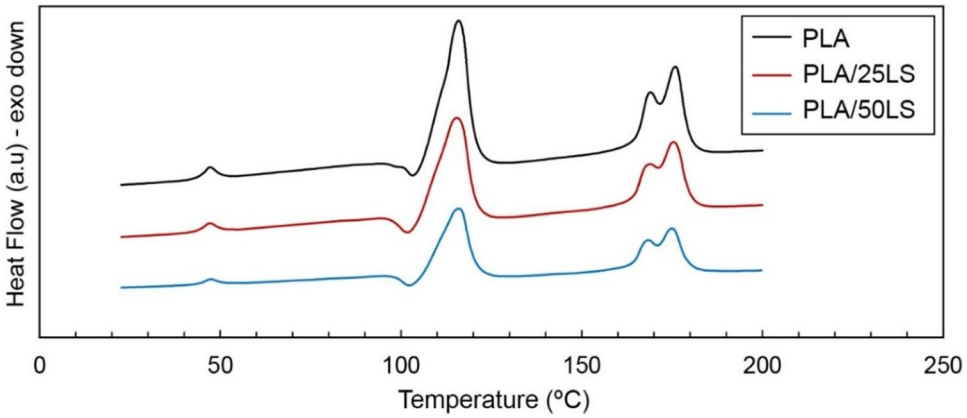

Fig. 3 Second heating thermograms obtained for PLA, PLA/25LS, and PLA/50LS

Table 3 Summary of transition temperatures, enthalpies, and degree of crystallinity according to material formulation

Material	T_{m1} (ºC)	ΔH_{m1}^* (J/g)	T_g (°C)	T_{cc} (ºC)	ΔH_{cc}^* (J/g)	T_{m2} (°C)	ΔH_{m2}^* (J/g)	T_{m3} (°C)	T_{m4} (°C)	$\Delta H_{m3,4}^*$ (J/g)	X_c (%)
PLA	47.2	1.3	60.0	103.3	1.8	115.9	30.5	168.9	175.8	23.4	57.4
PLA/25LS	47.3	1.2	67.0	102.9	2.9	115.5	32.4	168.9	175.3	26.3	61.4
PLA/50LS	47.4	1.2	55.6	102.4	3.2	115.9	30.5	168.4	174.9	23.1	55.5

* normalized values with respect to the theoretical PLA mass fraction

2.4 3D printing and tensile testing

The measured values of layer height and width were then used to adjust the slicing parameters so that tensile specimens with 100% infill could be printed. All specimens were printed using a print speed of 10 mm/s, nozzle temperature of 220 ºC, and bed temperature of 60 ºC, with rectilinear 0/90º raster. Slicing was configured to generate two perimeter shells, with no solid top or bottom layers. The specimens were positioned on the print bed in the C + 45 from XY orientation, as defined by ISO/ASTM F2971-13.

The tensile specimens, conforming to ISO/ASTM D638 type IV, were tested using an Instron 5566 equipped with a 10 kN load cell. The tests were conducted at room temperature with a crosshead speed of 2 mm/min, and a clamping length of 73.5 mm. Reported results represent the average of five independent measurements.

3 Results and discussion

3.1 Feedstock characterization

The second heating thermograms for neat PLA, PLA/25LS, and PLA/50LS are presented in Fig. 3. All materials exhibited a small endothermic peak below 50 °C, followed by a minor cold crystallization event near 100 °C, just preceding the main melting peak at approximately 115 °C. Finally, double endothermic transitions were observed, with peaks centered around 168 °C and 175 °C.

The key thermal properties derived from the DSC analysis, with enthalpy values normalized by the theoretical PLA mass fraction, are summarized in Table 3. The complete set of thermograms and the corresponding analysis are provided in the supplementary file.

The glass transition temperature (T_g) exhibits a non-monotonic dependence on limestone content, increasing from 60 °C for neat PLA to 67 °C for PLA/25LS and then decreasing to 55.6 °C for PLA/50LS. The T_g increase at 25 wt.% limestone indicates restricted segmental mobility of PLA chains, consistent with effective polymer–filler interfacial interactions that stiffen the amorphous phase. In contrast, the pronounced T_g depression at 50 wt.% suggests that excessive filler loading disrupts the continuity of the polymer matrix, reducing chain entanglement density.

The evolution of melting and cold-crystallization transitions further supports this interpretation by revealing competing nucleation and mobility effects as filler content increases. The low-temperature melting peak at ~ 47 °C, associated with poorly organized or metastable crystalline structures, decreases monotonically with limestone addition, while the cold-crystallization peak at ~ 103 °C increases steadily. This trend indicates that increasing filler content progressively suppresses crystallization during cooling, leaving a larger fraction of chains trapped in the amorphous state that can only reorganize upon reheating. These effects are consistent with reduced chain mobility during cooling, particularly at high filler loadings.

In contrast, the enthalpy of the higher-temperature melting peaks (~ 115 °C and the conjugated peaks at ~ 169–175 °C), corresponding to thicker and more stable lamellae, initially increase at 25 wt.% limestone, evidencing a clear heterogeneous nucleation effect of the filler. This is corroborated by the increase in crystallinity degree from 57.3% for

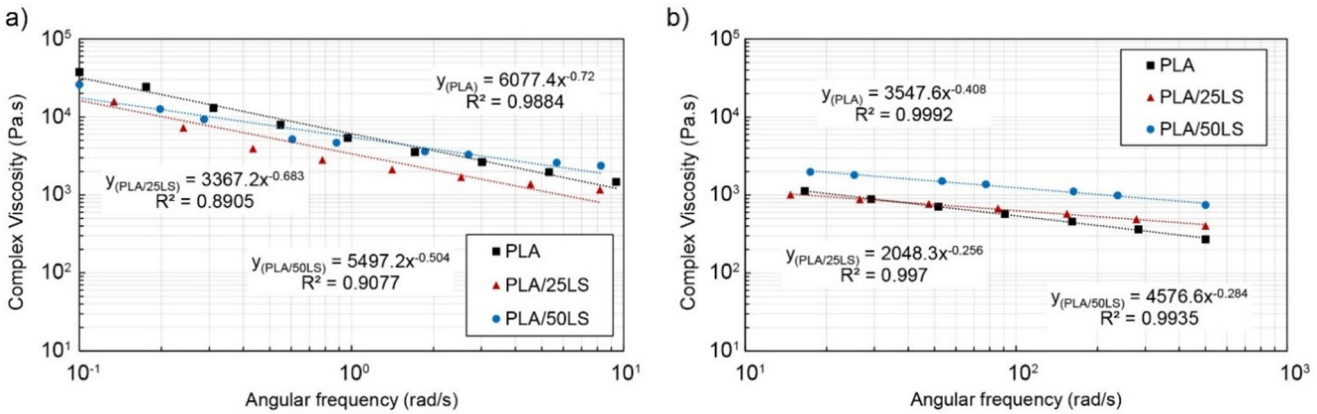

Fig. 4 Complex viscosity of PLA, PLA/25LS, and PLA/50LS at 200 ºC with angular frequency ranging from **a** 0.01 to 10 rad/s, and **b** 20 to 500 rad/s

Table 4 Power-law fitting parameters of the apparent viscosity in function of shear rate according to material

Material	$0.1 < \omega < 10$ rad/s		$20 < \omega < 500$ rad/s	
	K (Pa.s^n)	n	K (Pa.s^n)	n
PLA	6077.4	0.28	3547.6	0.59
PLA/25LS	3367.2	0.32	2048.3	0.74
PLA/50LS	5497.2	0.50	4576.6	0.72

neat PLA to 61.4% for PLA/25LS, indicating that at moderate filler content the polymer phase remains sufficiently continuous to allow chain diffusion and lamellar thickening. However, at 50 wt.% limestone, the enthalpy of these high-temperature melting peaks decrease, reflecting a transition to a mobility-limited, polymer-discontinuous regime in which particle–particle interactions dominate and hinder effective crystal growth [28]. Overall, the DSC results reveal a shift from a nucleation-dominated regime at intermediate filler loading to a mobility-controlled regime at high filler content, leading to delayed crystallization and reduced crystal perfection.

From the perspective of FPF, the increase in T_g and crystallinity observed for PLA/25LS is expected to promote earlier solidification and more rapid development of stiffness after deposition. This may improve dimensional stability and shape retention, but at the cost of a reduced time window for interlayer diffusion and molecular interpenetration, potentially weakening interlayer bonding. In contrast, the reduced T_g and lower crystallization observed for PLA/50LS imply earlier melt softening and a prolonged rubbery state. This behavior can enhance interlayer adhesion by allowing longer chain mobility and diffusion between layers, but at the expense of geometrical accuracy, increasing the risk of sagging or deformation during unsupported deposition.

Figure 4 presents the complex viscosity as a function of angular frequency for neat PLA, PLA/25LS, and PLA/50LS, all measured within the linear viscoelastic region (LVR) at a shear strain of 0.1%. Two distinct shear-thinning regimes are observed: (a) a regime with a higher slope at lower angular frequencies, ranging from 0.1 to 10 rad/s, and (b) a regime with a smaller slope at higher angular frequencies, from 20 to 500 rad/s. The corresponding power-law fitting equations and their associated R^2 values are also included.

As reflected by the power-law parameters summarized in Table 4, the lower flow index (n) observed at low angular frequencies for PLA/25LS and PLA/50LS indicates a particle-dominated rheological response, consistent with the highly filled nature of these composites. With increasing angular frequency, the fitted power-law exponents increase, indicating a reduction in shear-thinning intensity as polymer chain dynamics become more prominent. While the occurrence of two shear-thinning regimes is a well-documented feature of highly filled polymer melts [29], the absence of a Newtonian plateau at low angular frequencies for neat PLA is unexpected and suggests non-ideal melt behavior, requiring further investigation.

Figure 5 presents the storage modulus (G′) and loss modulus (G″) as functions of angular frequency. An unusual trend is observed in all materials, as the loss modulus exceeds the storage modulus over nearly the entire angular frequency range, indicating a predominantly viscous, liquid-like response. Typically, molten polymers and composites exhibit predominant elastic behavior at high shear rates [30]. This deviation appears inherent to the specific PLA grade used and may be attributed to a plasticizing effect of the PSAC within the PLA matrix. Only at very low angular frequencies does G′ approach or slightly surpass G″.

Table 5 summarizes the average crossover modulus (G_c), the corresponding angular frequency (ω_c), and the characteristic relaxation times ($\lambda = 1/\omega_c$) for the investigated materials. With increasing limestone content, G_c systematically shifts to lower angular frequencies, reflecting a progressive increase in relaxation times. This behavior is consistent with the high filler loading hypothesis, whereby particle–particle

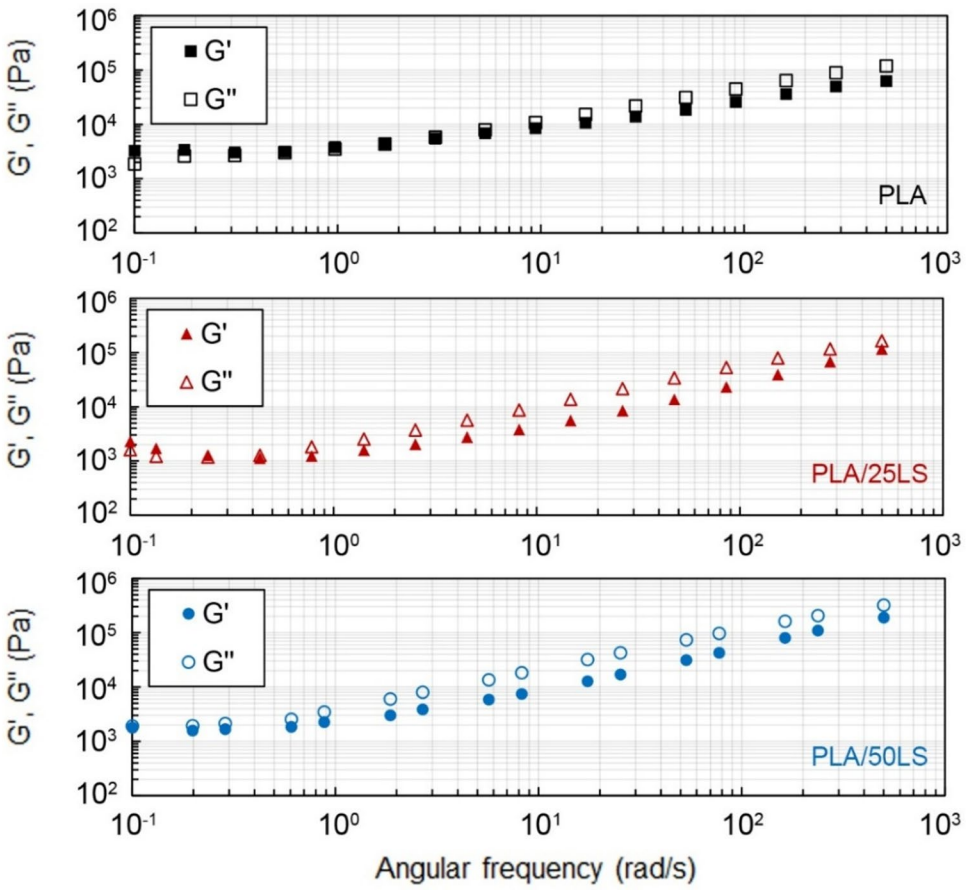

Fig. 5 Storage (G′) and loss (G″) modulus versus angular frequencies of PLA, PLA/25LS, and PLA/50LS at 200 ºC

Table 5 Average crossover modulus, frequency, and relaxation time of the PLA, PLA/25LS, and PLA/50LS

Material	G_c (Pa)	ω_c (rad/s)	λ (ms)
PLA	4290	1.71	584.79
PLA/25LS	1234	0.24	4166.67
PLA/50LS	1837	0.10	10,000

interactions and confinement effects hinder cooperative chain motion, leading to slower stress relaxation. At the same time, the effective continuity and entanglement density of the PLA phase are further reduced [31], preventing the development of a solid-like response even at low frequencies.

While higher ω (and thus higher shear rates) are more representative of the material's behavior within the extrusion unit during FPF, the lower-frequency data reflect the consolidation stage of the extruded filaments during 3D printing [16]. Although both composites are expected to exhibit higher viscosities than neat PLA within the screw channels, PLA/50LS displays significantly greater viscosity than PLA/25LS. At low angular frequencies, the reduction in complex viscosity observed for PLA/50LS may indicate insufficient shape retention after deposition. This is further corroborated by the narrowing frequency range in which G′ exceeds G″ as filler content increases.

Taken together with the DSC results, these findings suggest that excessive limestone content disrupts matrix continuity and polymer chain dynamics, ultimately altering the thermomechanical balance required for suitable FPF printability.

Figure 6 presents the FTIR spectra of the limestone powder, virgin PLA, and PLA recovered from the PLA/25LS and PLA/50LS composites after dilution and removal of the solid filler.

Two distinctive absorption peaks can be noticed in the limestone spectrum, one between 1400 and 1470 cm^{-1} and the other between 870 and 880 cm^{-1}, which correspond to the asymmetric stretch and out of plane flexion of carbonate group (CO_3^{2-}) [32].

Characteristic absorption bands in the virgin PLA are clearly observed, including the sp^3 C–H asymmetric and symmetric stretching vibrations at 2995 and 2950 cm^{-1}, the strong ester carbonyl (C=O) stretching at 1750 cm^{-1}, C–H bending modes at 1450 and 1340 cm^{-1}, and the C–O–C stretching vibrations in the region between 1260 and 1050 cm^{-1} [33–35]. In the composite samples, slight reductions of the C–H stretching (~2950 cm^{-1}), C=O stretching (~1750 cm^{-1}), C–H bending (~1450 cm^{-1}), and C–O–C stretch (~1180–1120 cm^{-1}) peaks were observed [36].

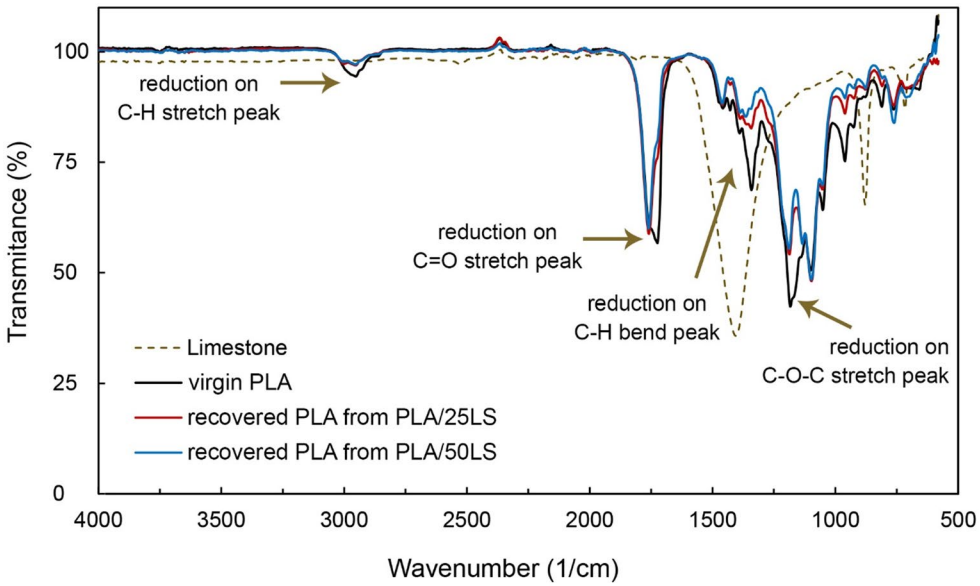

Fig. 6 FTIR spectra of limestone, virgin PLA, and PLA recovered from both PLA/25LS and PLA/50LS composites

With respect to the FTIR spectra of PLA recovered from the composites, the characteristic limestone bands are, as expected, not observed, thereby avoiding overlapping or masking of PLA-related absorption bands. The rationale for recovering the PLA matrix from the composites was to assess compounding-induced alterations that could affect the thermal and rheological properties of the matrix. Nevertheless, the main limitation of this approach is that it does not capture or directly evaluate filler–matrix interactions within the composites.

Only minor variations in band intensity are observed in the spectra of the recovered PLA when compared to virgin PLA, particularly in the regions associated with C–H stretching (~2950 cm^{-1}), C=O stretching (~1750 cm^{-1}), C–H bending (~1450 cm^{-1}), and C–O–C stretching (~1180–1120 cm^{-1}). These differences are subtle and do not indicate significant chemical modification of the polymer backbone. In this context, the absence of increased absorption in the 3500–3200 cm^{-1} region, for example, suggests that hydrolytic degradation of the PLA matrix during processing was negligible [37]. Finally, no significant differences are observed between the spectra of PLA recovered from the PLA/25LS and PLA/50LS composites, indicating that thermomechanical processing under intermediate or high filler loadings did not lead to detectable alterations in the FTIR response of the recovered PLA.

3.2 FPF parameters calibration

The initial screening tests indicated that extrusion was only feasible at 200 ºC for feed rates up to 10 mm/s. Significant motor stalling was observed at this temperature, particularly with the composites, but also with neat PLA at higher feed rates. At 220 ºC and 240 ºC, successful extrusion was achieved with all feed rates tested. Motor stalling at lower temperatures and higher feed rates can be attributed to insufficient torque to convey and compact the pellets in the compression zone of the screw, where plastication typically begins. Although increasing the feed rate would generate higher shear rates, potentially promoting flow thought shear-thinning, the heat transference from barrel to polymer may not have been fast enough to fully melt the PLA phase.

Figure 7 presents the volumetric flow rate measurements for each material under feasible extrusion conditions, with feed rates of 10, 20, and 30 mm/s and nozzle temperatures of 220 °C and 240 °C, as well as the corresponding specific throughputs, i.e. screw-speed–normalized volumetric flow rates, for both temperatures. The rotational speed of the screw was determined by measuring the extruder motor speed in revolutions per minute and dividing this value by five to account for the gearbox reduction.

The basic theory of melt conveying in single-screw extrusion expresses the volumetric flow rate as shown in Eq. 2 [38], resulting from the combined contributions of a drag-induced flow, which is proportional to the screw speed (N), and a pressure-induced counterflow, which is proportional to the pressure gradient and melt viscosity (ΔP/η). In this formulation, A and B are geometric constants related to the screw and channel geometry.

$$\dot{V}_{screw} = AN - B\frac{\Delta P}{\eta} \tag{2}$$

As predicted by Eq. 2, a linear relationship was observed between volumetric flow rate and feed rate (*i.e.*, screw speed) for each material at both temperatures. However, the absolute flow rate systematically decreased with increasing filler content. The specific throughput provides a clear

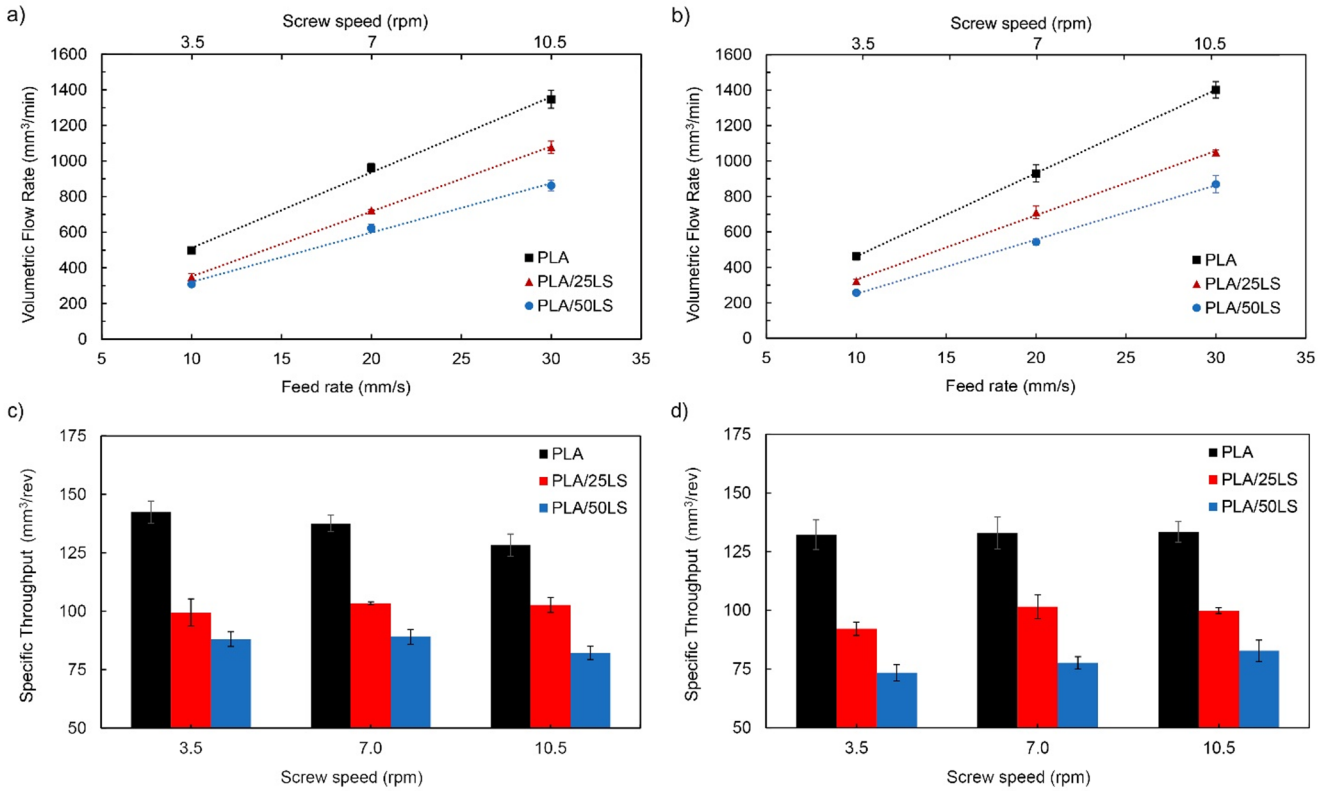

Fig. 7 Volumetric flow rates of PLA, PLA/25LS, and PLA/50LS measured at different feed rates and nozzle temperatures of **a** 220 °C and **b** 240 °C; corresponding specific throughputs at **c** 220 °C and **d** 240 °C

indication of the influence of melt viscosity on volumetric flow behavior, with lower values reflecting more significant pressure-induced counterflow associated with higher viscosity. The effect of increasing limestone content is evident and is consistent with the higher complex viscosity values measured for the composites at angular frequencies above 100 rad s^{-1}.

Minor variations in specific throughput with screw speed for a given material can be attributed to competing effects. On one hand, increased viscous dissipation at higher screw speeds may locally reduce melt viscosity and pressure gradients, leading to a slight increase in net throughput. On the other hand, higher pressure levels associated with increased screw speeds can promote material leakage through the clearance between the screw flight and the barrel. Both effects are not accounted for in the simplified model of Eq. 2.

Feed rate had a statistically significant influence on volumetric throughput for all materials ($p<0.001$). Nozzle temperature was statistically significant only for PLA/25LS ($p=0.035$) and PLA/50LS ($p=0.001$), with higher temperatures leading to slightly lower flow rates. A significant interaction between feed rate and temperature was also observed for PLA ($p=0.046$) and PLA/50LS ($p=0.009$). The corresponding ANOVA tables are provided in the supplementary file.

The 20 mm cubes printed with neat PLA to determine the appropriate EM are shown in Fig. 8.

At both print speed levels, EM of 1 and 2 were insufficient to produce continuous walls with well-defined strands. It is evident that an extrusion multiplier of 1 (typically adequate for PLA in conventional FFF 3D printing) is not suitable for the FPF hardware employed, as the screw motor must rotate faster than it would for filamentary feedstock in the same printing conditions. While the cubes printed at 10 mm/s with multipliers of 3 and 4 presented good overall quality, those printed at 30 mm/s exhibited curled corners, with the deformation being more distinct when a multiplier of 4 was used. These curled corners, which appeared mainly in the upper portion of the cubes at the point where the nozzle starts a new layer, are attributed to the structure's inability to cool and solidify fast enough at higher print speeds. The localized thermal accumulation is exacerbated by increased material flow, hindering solidification and resulting in significantly distorted geometries.

Figure 9 shows the cubes printed with PLA, PLA/25LS, and PLA/50LS using PS of 10 and 30 mm/s and EM of 3 and 4. Approximately half of the fractured walls are displayed

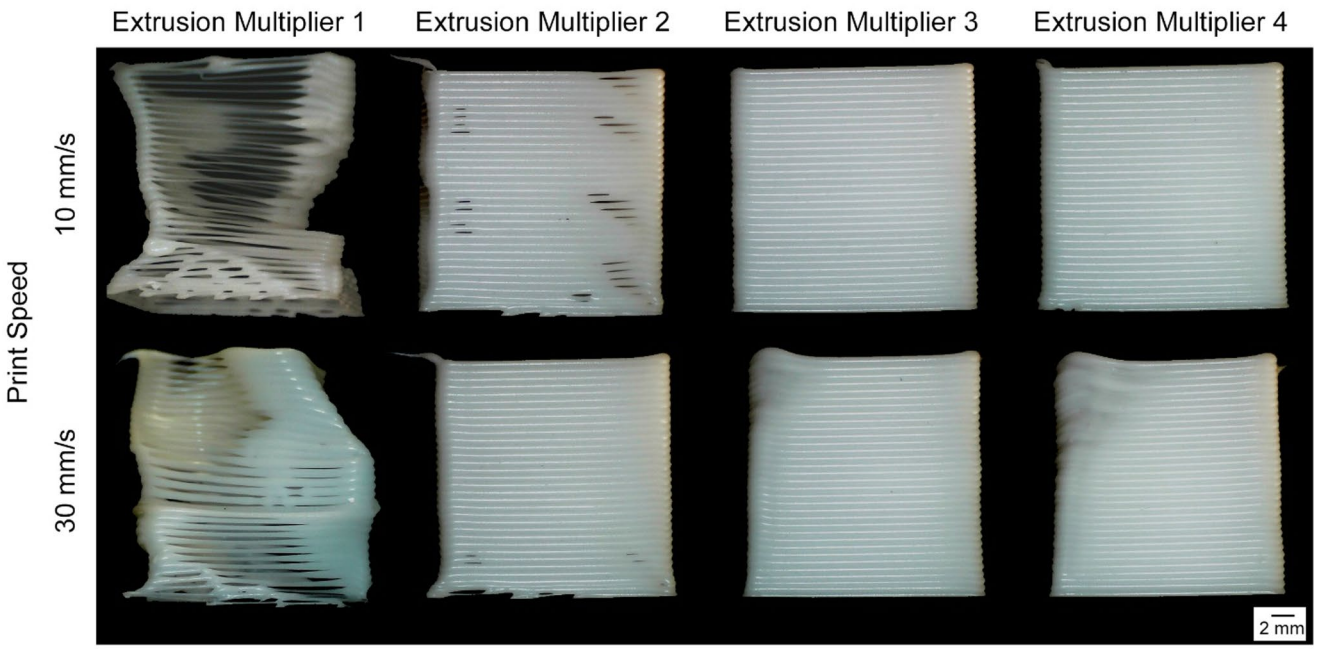

Fig. 8 Side view of the cubes printed with neat PLA in vase mode with print speed of 10 mm/s and 30 mm/s, and varying EM from 1 to 4

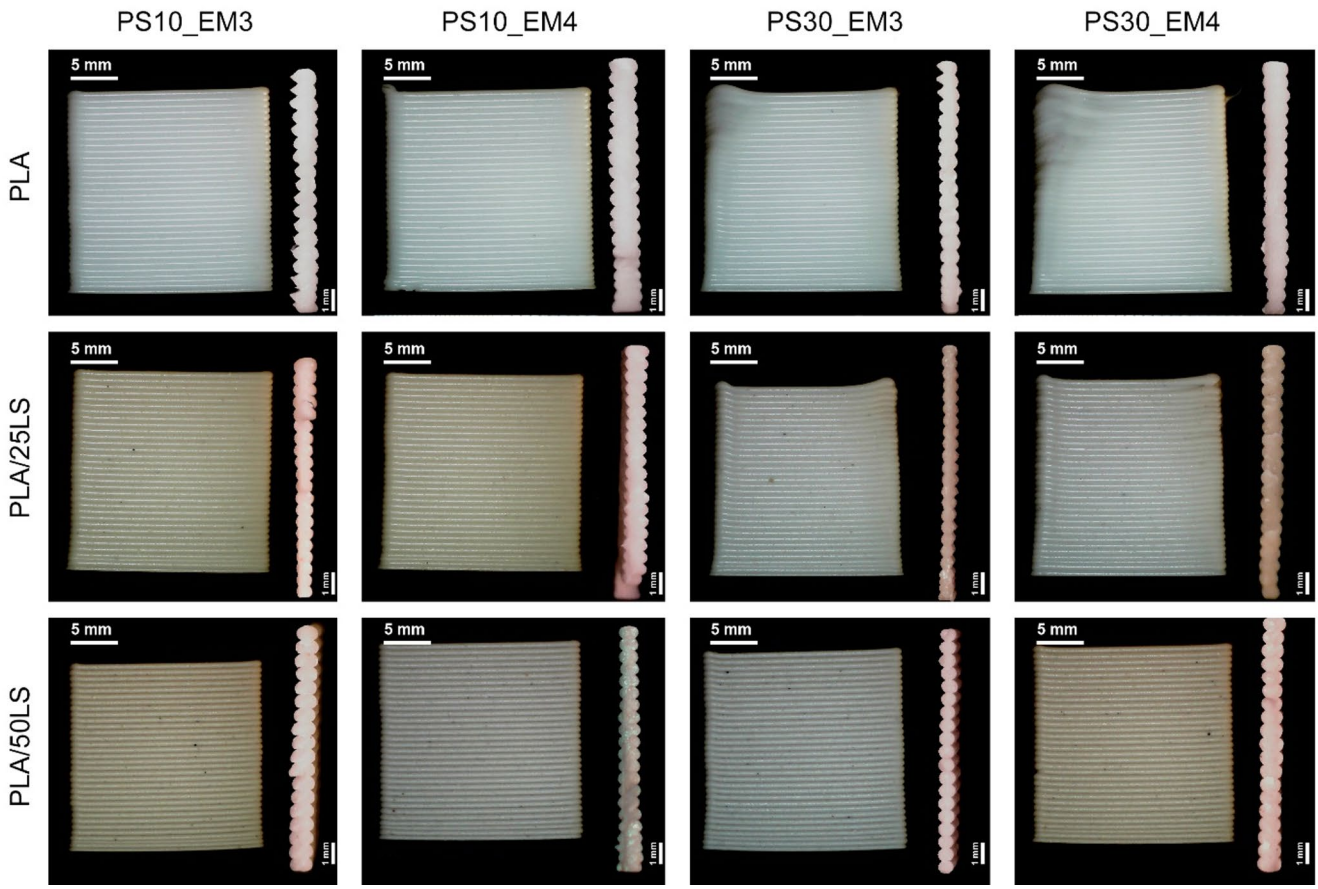

Fig. 9 Side view of the calibrations cubes and corresponding fractured walls printed with PLA, PLA/25LS, and PLA/50 LS pellets at 10 and 30 mm/s PS and with EM of 3 and 4

alongside their corresponding cubes, highlighting the differences in the geometry of the deposited strands.

While all cubes printed at 10 mm/s exhibited good overall quality, slight deformations in the upper layers were still observed in the PLA/25LS samples printed at 30 mm/s. In terms of shape fidelity, the increased thermal conductivity and higher viscosity of the PLA/50LS composite as it leaves the nozzle appears to reduce corner curling caused by localized thermal accumulation.

The measured layer heights (h) and extrusion widths (w) obtained from the fractured walls of the calibration cubes are presented in Fig. 10, color-coded by material and grouped according to the printing conditions. The corresponding statistical analysis is presented in thesupplementary file.

For neat PLA, PS was the only factor with a statistically significant effect on h ($p<0.001$), leading to a reduction in layer height with increasing speed. In contrast, for PLA/25LS and PLA/50LS, EM was the dominant factor affecting h ($p<0.001$), with opposite trends: increasing EM increased h in PLA/25LS but decreased h in PLA/50LS. For PLA/50LS, the interaction (PS x EM) was also statistically significant ($p<0.001$), revealing a cross-over interaction in which the effect of EM on the response depends on the level of PS. Anyway, the response of h was always around 0.6 mm owing to the nozzle-to-bed distance, aligning with the literature [39].

A stronger influence on w was observed within the tested printing parameters. EM and PS were statistically significant ($p<0.001$) for PLA, and PLA/50LS, while for PLA/25LS only EM has significant influence ($p<0.001$) on layer width. The influence of the interaction PS × EM was significant across all materials ($p<0.005$). Increasing EM generally led to wider extruded strands, while increasing PS resulted in narrower ones. Layer width was more sensitive to PS than to EM for PLA and PLA/50LS. Additionally, increasing limestone content tended to reduce w, particularly at lower printing speeds (10 mm/s) and higher extrusion multipliers (EM = 4).

3.3 3D printed tensile specimens and mechanical properties

The test specimens were printed using the average values of layer height (h) and extrusion width (w) obtained under the PS10_EM3 printing condition. This condition was selected because, at this print speed, PLA exhibited a lower tendency to deform due to heat accumulation (Fig. 9) and showed reduced variability in the resulting layer width compared to PS10_EM4 (Fig. 10). However, this choice does not imply that the selected parameters represent optimal printing conditions, as a comprehensive mapping of the effects of PS and EM on the resulting mesostructure was beyond the scope of this study. Moreover, even a calibration aimed at achieving a nominally 100% dense mesostructure does not necessarily yield optimal mechanical properties, since sub-voxel material characteristics, such as local crystallinity, may be significantly influenced by the printing conditions.

Based on the PS10_EM3 condition, tensile specimens were printed with a nominal layer height of 0.6 mm and an extrusion width of 1.1 mm using PLA, PLA/25LS, and PLA/50LS pellets under the selected conditions. The printed specimens are shown in Fig. 11, and the corresponding stress–strain curves are presented in Fig. 12.

The stress–strain curves indicate that the incorporation of limestone increased the stiffness of the material, particularly in the PLA/50LS composites, which was accompanied by

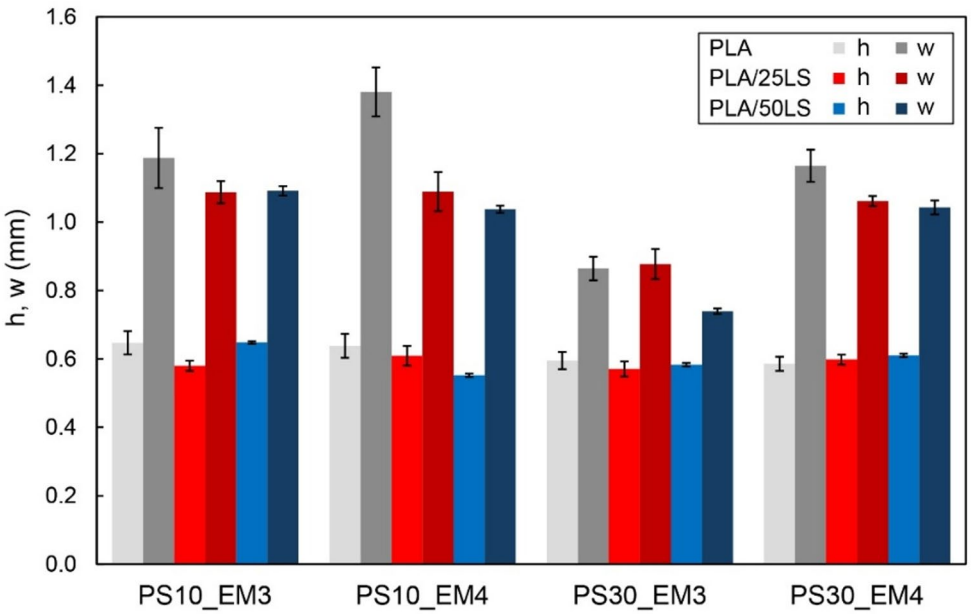

Fig. 10 Layer height (h) and width (w) measured from the fractured walls of the calibration cubes for PLA, PLA/25LS, and PLA/50LS printed at 10 and 30 mm/s with EM of 3 and 4

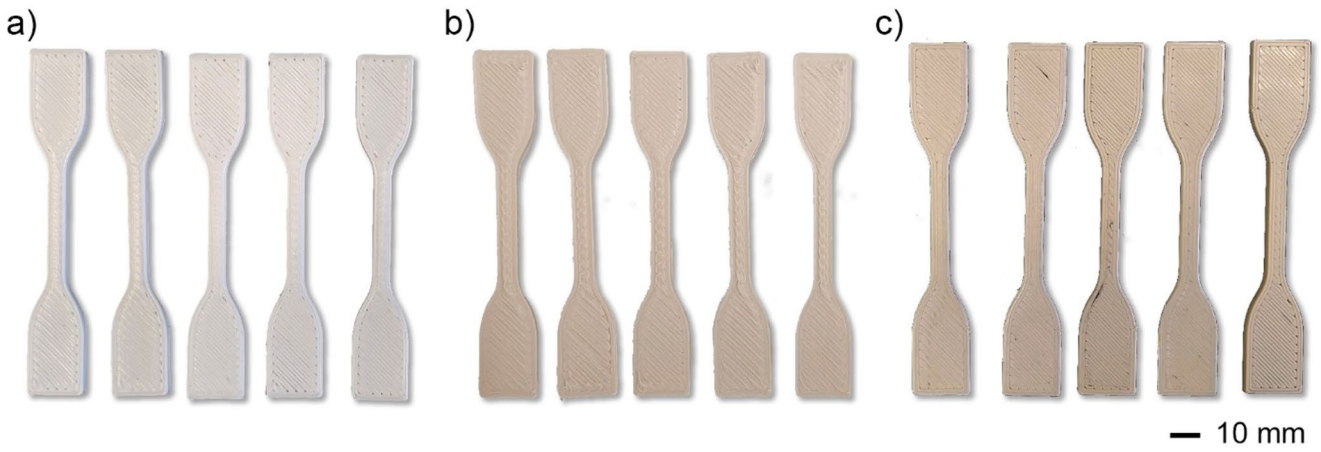

Fig. 11 Tensile specimens printed with **a** PLA, **b** PLA/25LS, and **c** PLA/50LS

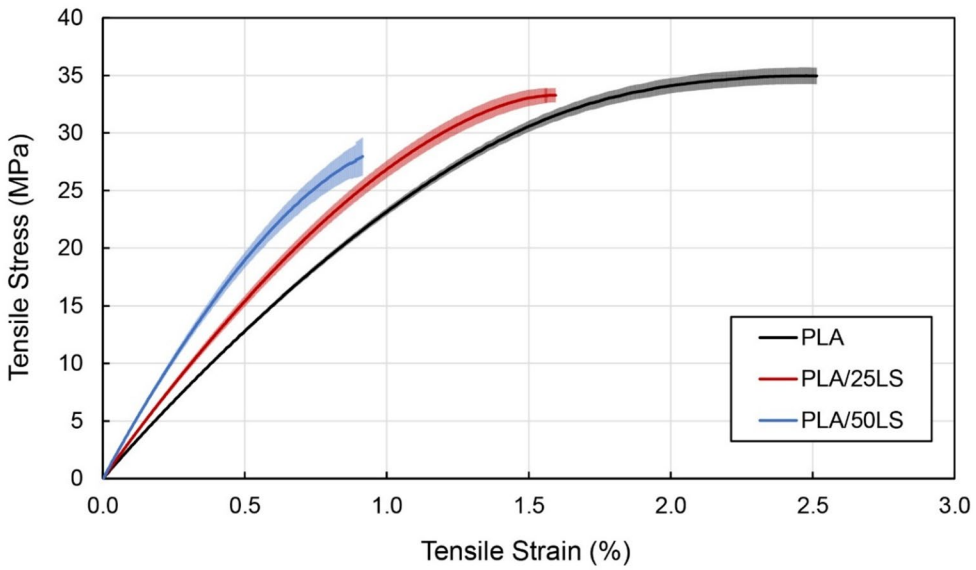

Fig. 12 Tensile stress versus strain curves obtained for the 3D printed specimens

Table 6 Summary of the mechanical properties of the tensile specimens printed with PLA, PLA/25LS, and PLA/50LS pellets

Material	Modulus (GPa)	Stress at break (MPa)	Elongation at break (%)
PLA	2.55 ± 0.33	34.95 ± 0.69	2.51 ± 0.06
PLA/25LS	3.23 ± 0.06	33.29 ± 0.62	1.59 ± 0.02
PLA/50LS	4.32 ± 0.25	28.06 ± 1.57	0.95 ± 0.07

a corresponding decrease in stress and elongation at break. The mechanical properties are summarized in Table 6 for each material formulation. Variability in modulus was lowest for PLA/25LS, followed by PLA/50LS and neat PLA, while variability in stress and elongation at break was also smallest for PLA/25LS, followed by neat PLA and then PLA/50LS.

In a previous study, Sousa et al. [13] processed the same pellets into 3D printing filaments, printed tensile specimens, and conducted tensile tests. The reported values for PLA (2.5 GPa modulus, 30 MPa stress at break, and 1.7% strain at break), PLA/25LS (3 GPa modulus, 30 MPa stress at break, and 1.6% strain at break), and PLA/50LS (4.2 GPa modulus, 26.8 MPa stress at break, and 0.8% strain at break) are in good agreement with the results shown in Table 6, except for the strain values at break, which were consistently smaller.

4 Conclusions

In this study, the properties of neat PLA and composite pellets containing 25 wt.% and 50 wt.% limestone were evaluated to assess their suitability for FPF processing. The investigation covered thermal behavior, rheological response, and potential structural changes induced by compounding. Based on these results, a three-stage FPF calibration process was conducted for each material formulation

using a retrofitted 3D printer equipped with a miniature screw extruder.

The main conclusions are summarized as follows:

- Feedstock characterization suggests that limestone content alters PLA chain mobility, crystallization kinetics, and melt dynamics. At 25 wt.% limestone, effective polymer–filler interactions increase T_g and crystallinity, indicating a still-continuous PLA matrix with enhanced heterogeneous nucleation. In contrast, 50 wt.% limestone pushes the system into a polymer-discontinuous regime: T_g decreases, crystallization during cooling is suppressed, and relaxation times increase markedly. Rheologically, this is reflected in stronger particle-dominated behavior at low frequencies, higher viscosity in the screw, and slower stress relaxation. Despite the additional thermomechanical process required to fabricate the composite pellets, there was no significant signal of PLA degradation.
- The extrusion screening tests and calibration cubes clearly demonstrate that FPF processing parameters differ from those typically used in FFF. Formulation-dependent flow behavior, particularly the increase in viscosity with filler loading at higher angular frequencies, results in reduced volumetric flow rates due to increased pressure-induced backflow within the extruder. In contrast, variations in solidification and crystallization behavior were more difficult to directly relate to printing quality. Instead, thermal conductivity, although not directly monitored, was found to exert a more pronounced influence on print quality.
- Nonetheless, the three-stage calibration strategy proved effective in establishing suitable, though not optimal, adjustment factors for h, w, and EM, enabling successful fabrication of tensile specimens. Quasi static tensile testing revealed increased stiffness and reduced ductility with increasing limestone content, with elastic modulus, tensile strength, and strain at break values consistent with those reported for the same materials processed by FFF.
- From a sustainability standpoint, although the full processing route may be energy-intensive, further improvements in equipment design and process optimization for large-scale applications may provide a feasible pathway for the valorization of stone industry residues while reducing reliance on virgin synthetic polymer production. A detailed life cycle assessment under industrially relevant conditions is recommended to fully validate the environmental benefits of the proposed approach.

Supplementary Information The online version contains supplementary material available at https://doi.org/10.1007/s40964-026-01567-1.

Acknowledgements The authors acknowledge Fundação para a Ciência e a Tecnologia (FCT) for its financial support via LAETA (project https://doi.org/10.54499/UID/50022/2025). The authors would like to thank the project Sustainable Stone by Portugal—Valorization of Natural Stone for a digital, sustainable and qualified future, nº 40, proposal nº C644943391-00000051, co-financed by PRR—Recovery and Resilience Plan of the European Union (Next Generation EU). This work has also been supported by the European Union under the Next Generation EU, through a grant of the Portuguese Republic's Recovery and Resilience Plan (PRR) Partnership Agreement, within the scope of the project PRODUTECH R3 "Agenda Mobilizadora da Fileira das Tecnologias de Produção para a Reindustrialização," aiming the mobilization of the production technologies industry towards of the reindustrialization of the manufacturing industrial fabric (Project ref. nr. 60-C645808870—00000067). The authors would also like to thank CDRSP-IPLeiria and Filstone—Comércio de Rochas S.A. for the limestone powder.

Author contributions Conceptualization, J.M.J.N., P.A., M.L.; methodology, J.M.J.N., D.S.; formal analysis, J.M.J.N., D.S.; investigation, J.M.J.N., D.S.; resources, D.S., P.A.; data curation, J.M.J.N., D.S.; writing—original draft preparation, J.M.J.N., D.S.; writing—review and editing, J.M.J.N., D.S., M.L., P.A.; visualization, J.M.J.N.; supervision, M.L., P.A.; project administration, M.L., P.A.; funding acquisition, M.L., P.A.

Funding Open access funding provided by FCT|FCCN (b-on).

Data availability No datasets were generated or analysed during the current study.

Declarations

Conflict of interest The authors declare no competing interests.

References

1. Portugal Business News, "Portugal ranks 7th largest producer of natural stone in the world". https://www.portugalbusinessesnews.com/post/portugal-ranks-7th-largest-producer-of-natural-stone-in-the-world. Accessed on July 22, 2025.
2. Careddu N, Dino GA (2016) Reuse of residual sludge from stone processing: differences and similarities between sludge coming from carbonate and silicate stones—Italian experiences. Environ Earth Sci 75(14):1075. https://doi.org/10.1007/s12665-016-5865-1
3. Fu SY, Feng XQ, Lauke B, Mai YW (2008) Effects of particle size, particle/matrix interface adhesion and particle loading on

mechanical properties of particulate-polymer composites. Compos Part B Eng 39(6):933–961. https://doi.org/10.1016/j.compositesb.2008.01.002
4. Fajdek-Bieda A, Wróblewska A (2024) The use of natural minerals as reinforcements in mineral-reinforced polymers: a review of current developments and prospects. Polymers. https://doi.org/10.3390/polym16172505
5. Kashyap S, Datta D (2017) Reusing industrial lime sludge waste as a filler in polymeric composites. Mater Today Proc. https://doi.org/10.1016/j.matpr.2017.02.176
6. Barczewski M, Sałasińska K, Kloziński A, Skórczewska K, Szulc J, Piasecki A (2019) Application of the basalt powder as a filler for polypropylene composites with improved thermo-mechanical stability and reduced flammability. Polym Eng Sci 59(s2):E71–E79. https://doi.org/10.1002/pen.24962
7. Awad AH, El-gamasy R, Abd El-Wahab AA, Hazem Abdellatif M (2019) Mechanical behavior of PP reinforced with marble dust. Constr Build Mater. https://doi.org/10.1016/j.conbuildmat.2019.116766
8. Lendvai L, Singh T, Fekete G, Patnaik A, Dogossy G (2021) Utilization of waste marble dust in poly(lactic acid)-based biocomposites: mechanical, thermal and wear properties. J Polym Environ 29(9):2952–2963. https://doi.org/10.1007/s10924-021-02091-9
9. de Sousa GS, da Silva GD, d'Almeida JR (2021) Influence of soapstone waste on the mechanical and rheological properties of high-density polyethylene. J Appl Polym Sci. https://doi.org/10.1002/app.50966
10. Romani A, Suriano R, Levi M (2023) Biomass waste materials through extrusion-based additive manufacturing: a systematic literature review. J Clean Prod 386:135779. https://doi.org/10.1016/J.JCLEPRO.2022.135779
11. Romani A, Rognoli V, Levi M (2021) Design, materials, and extrusion-based additive manufacturing in circular economy contexts: from waste to new products. Sustainability 13(13):7269. https://doi.org/10.3390/SU13137269
12. Esposito Corcione C, Palumbo E, Masciullo A, Montagna F, Torricelli MC (2018) Fused deposition modeling (FDM): an innovative technique aimed at reusing lecce stone waste for industrial design and building applications. Constr Build Mater 158:276–284. https://doi.org/10.1016/j.conbuildmat.2017.10.011
13. Sousa D, Baleia C, Amaral P (2025) PLA reinforced with limestone waste: a way to sustainable polymer composites. Polymers. https://doi.org/10.3390/polym17050662
14. Justino Netto JM, Idogava HT, Frezzatto Santos LE, de C. Silveira Z, Romio P, Alves JL (2021) Screw-assisted 3D printing with granulated materials: a systematic review. Int J Adv Manuf Technol 115:2711–2727. https://doi.org/10.1007/s00170-021-07365-z
15. Bozorgnia Tabary SAA, Bresse JP, Fayazfar H (2017) From waste to function: Compatibilized r-PET/r-HDPE blends for pellet extrusion 3D printing. Polymers 17(12):1638. https://doi.org/10.3390/polym17121638
16. Das A, Gilmer EL, Biria S, Bortner MJ (2021) Importance of polymer rheology on material extrusion additive manufacturing: correlating process physics to print properties. ACS Appl Polym Mater. https://doi.org/10.1021/acsapm.0c01228
17. La Gala A, Fiorio R, Erkoç M, Cardon L, D'hooge DR (2020) Theoretical evaluation of the melting efficiency for the single-screw micro-extrusion process: the case of 3D printing of abs. Processes 8(11):1–22. https://doi.org/10.3390/pr8111522
18. Martin V, Witz JF, Gillon F, Najjar D (2022) Low cost 3D printing of metals using filled polymer pellets specifications table. HardwareX 11:292. https://doi.org/10.5281/zenodo.5484803
19. Curmi A, Rochman A, Gatt A (2024) Screw extrusion additive manufacturing of thermoplastic polyolefin elastomer. Prog Addit Manuf 10:1161–1174
20. RepRap, "G-code". https://reprap.org/wiki/G-code. Accessed on July 22, 2025.
21. Curmi A, Rochman A (2024) Miniaturized fused granulate fabrication of polyether ether ketone (PEEK). Prog Addit Manuf 9:1265–1275. https://doi.org/10.1007/s40964-023-00518-4
22. Sola A (2022) Materials requirements in fused filament fabrication: a framework for the design of next-generation 3d printable thermoplastics and composites. Macromol Mater Eng. https://doi.org/10.1002/MAME.202200197
23. "This is the free Material Data Center Datasheet of Inzea® F2 - (PLA+PSAC) - Nurel S.A." https://www.materialdatacenter.com/ms/pt/tradenames/Inzea/Nurel+S%252EA/Inzea%C2%AE+F2+HTS+655/18ae20f5/7279. Accessed on 22 July 2025.
24. Song Y, Li Y, Song W, Yee K, Lee KY, Tagarielli VL (2017) Measurements of the mechanical response for unidirectional 3D printed PLA. Mater Des 123:154–164. https://doi.org/10.1016/j.matdes.2017.03.051
25. Mahor.XYZ, "Pellet Extruder wiki", 2025. https://mahor.xyz/wiki/pellet-extruder-wiki/. Accessed on 22 July 2025.
26. Ajjarapu KPK, Mishra R, Malhotra R, Kate KH (2024) Mapping 3D printed part density and filament flow characteristics in the material extrusion (MEX) process for filled and unfilled polymers. Virtual Phys Prototyp. https://doi.org/10.1080/17452759.2024.2331206
27. Serra-Parareda F, Alba J, Tarrés Q, Espinach FX, Mutjé P, Delgado-Aguilar M (2021) Characterization of CaCO3 filled poly(lactic) acid and bio polyethylene materials for building applications. Polymers 13:3323. https://doi.org/10.3390/polym13193323
28. Ren Z, Shanks RA, Rook TJ (2001) Crystallization and melting of highly filled polypropylene composites prepared with surface-treated fillers. J Appl Polym Sci 79(11):1942–1948. https://doi.org/10.1002/1097-4628(20010314)79:11%3c1942::AID-APP1001%3e3.0.CO;2-P
29. Kukla C, Duretek I, Gonzalez-Gutierrez J, Holzer C (2018) Rheology of highly filled polymers. Polym Rheol. https://doi.org/10.5772/intechopen.75656
30. Acierno D, Patti A (2023) Fused deposition modelling (FDM) of thermoplastic-based filaments: process and rheological properties - an overview. Materials. https://doi.org/10.3390/ma16247664
31. Rueda MM, Auscher MC, Fulchiron R, Périé T, Martin G, Sonntag P, Cassagnau P (2017) Rheology and applications of highly filled polymers: a review of current understanding. Prog Polym Sci 66:22–53. https://doi.org/10.1016/j.progpolymsci.2016.12.007
32. Faba S, Agüero A, Arrieta MP, Martínez S, Romero J, Torres A, Galotto MJ (2024) Foaming of 3D-printed PLA/CaCO3 composites by supercritical CO2 process for sustainable food contact materials. Polymers 16(6):798. https://doi.org/10.3390/polym16060798
33. de Souza Meiros CB, Silva BL, Medeiros AM, Melo JDD, Barbosa APC (2024) Degradation of 3D-printed poly(lactic acid) for biomedical applications. Polym Bull 81(7):6271–6281. https://doi.org/10.1007/s00289-023-04992-2
34. Chieng BW, Ibrahim NA, Yunus WMZW, Hussein MZ, Z. M (2014) Poly(lactic acid)/Poly(ethylene glycol) polymer nanocomposites: effects of graphene nanoplatelets. Polymers 6(1):93–104. https://doi.org/10.3390/polym6010093
35. Chopra S, Pande K, Puranam P, Deshmukh AD, Bhone A, Kale R, Galande A, Mehtre B, Tagad J, Tidakea S (2023) Explication of mechanism governing atmospheric degradation of 3D-printed poly(lactic acid) (PLA) with different in-fill pattern and varying

in-fill density. RSC Adv 13(11):7135–7152. https://doi.org/10.1039/d2ra07061h
36. Vălean C, Linul E, Palomba G, Epasto G (2024) Single and repeated impact behavior of material extrusion-based additive manufactured PLA parts. J Mater Res Technol 30:1470–1481. https://doi.org/10.1016/j.jmrt.2024.03.150
37. Shi X, Jiang J, Sun L, Gan Z (2011) Hydrolysis and biomineralization of porous PLA microspheres and their influence on cell growth. Colloids Surf B Biointerfaces 85(1):73–80. https://doi.org/10.1016/j.colsurfb.2010.11.016
38. M. J. Stevens, J. A. Covas, Extruder Principles and Operation, 2nd ed. New Delhi: Springer Science+Business Media, B. V., 1995.
39. Jang S, Boddorff A, Jang DJ, Lloyd J, Wagner K, Thadhani N, Brettmann B (2021) Effect of material extrusion process parameters on filament geometry and inter-filament voids in as-fabricated high solids loaded polymer composites. Addit Manuf 47:102313. https://doi.org/10.1016/J.ADDMA.2021.102313